IEEE Access
Multidisciplinary | Rapid Review | Open Access Journal

Received May 10, 2019, accepted June 14, 2019, date of publication June 24, 2019, date of current version July 17, 2019.

*Digital Object Identifier 10.1109/ACCESS.2019.2924710*

# Toward Quantitative Near Infrared Brain Functional Imaging: Lock-In Photon Counting Instrumentation Combined With Tomographic Reconstruction

**DONGYUAN LIU[1], BINGYUAN WANG[1], TIANTIAN PAN[1], JIAO LI[1,2], ZHUANPING QIN[3], LIMIN ZHANG[1,2], ZHONGXING ZHOU[1,2], AND FENG GAO[1,2]**

[1]College of Precision Instruments and Optoelectronics Engineering, Tianjin University, Tianjin 300072, China
[2]Tianjin Key Laboratory of Biomedical Detecting Techniques and Instruments, Tianjin 300072, China
[3]School of Automation and Electrical Engineering, Tianjin University of Technology and Education, Tianjin 300222, China

Corresponding author: Feng Gao (gaofeng@tju.edu.cn)

This work was supported in part by the National Natural Science Foundation of China under Grant 61575140, Grant 81871393, Grant 61475116, Grant 61475115, Grant 81671728, Grant 81571723, and Grant 81771880, and in part by the Tianjin Municipal Government of China under Grant 17JCQNJC12700, Grant 17JCZDJC32700, and Grant 18JCYBJC29400.

**ABSTRACT** It is well acknowledged that the functional near-infrared spectroscopic (fNIRS) imaging of brain functions can be quantitatively enhanced by diffuse optical tomography (DOT). Unlike the widely-used conventional optical topography (optical mapping), an fNIRS-DOT instrument needs to possess both high sensitivity and large dynamic-range so that measurements at multiple source-detector separations are reliably and synchronously collected for improved depth-resolution, quantitation, and superficial signal reduction, the performances particularly crucial to the occipital cortex probing. For the goal, we implemented a novel 3-wavelength, 240-channel (20 sources and 12 detectors) continuous-wave fNIRS-DOT instrument. The system features the square-wave modulation lock-in photon-counting scheme that combines the multi-channel parallelization of the lock-in detection, the ultra-high sensitivity, and unprecedented dynamic-range of the photon-counting technique, as well as the reduced complexity of the hardware architecture. We have systematically investigated the key specifications of the instrument such as the detection linearity, stability, channel crosstalks and so on, under the practically-viable conditions of the incident power and signal-to-noise ratio, and accordingly proposed wavelength-switched multiple-field illumination paradigms for both the non-overlapping and overlapping DOT measurements, respectively. Finally, DOT experiments using the semi-three-dimensional image reconstruction has been conducted on a phantom with a practically low-contrasted and deep-sit absorption target, to evaluate the overall imaging performance of the system and to demonstrate the superiority of the model-based image reconstruction over the topographical mapping.

**INDEX TERMS** Functional near-infrared spectroscopic imaging, diffuse optical tomography, square-wave modulation, lock-in photon-counting.

## I. INTRODUCTION

Functional near-infrared spectroscopic (fNIRS) imaging mainly originates from the Jobsis' research that near-infrared photons can penetrate several centimeters through tissue and still be detected [1]. This technique is specifically suitable for functional neuroimaging due to the neural and hemodynamic coupling mechanism, where backscattered fNIRS signals from beneath the brain surface, including skin, skull and cerebrospinal fluid (CSF) layers, are measured at multi-wavelengths to recover the temporal changes of oxy-hemoglobin (HbO) and deoxy-hemoglobin (Hb) concentrations and further to quantitatively analyze the cortical hemodynamic response to neural activation [2]–[4]. Over the other neuroimaging modalities such as functional magnetic resonance imaging (fMRI), positron emission tomography (PET), electroencephalography (EEG), and magnetencephalography (MEG), fNIRS-imaging possesses concurrent advantages of non-invasiveness, high temporal resolution, experimental flexibility, electromagnetic

The associate editor coordinating the review of this manuscript and approving it for publication was Xiaodong Yang.

  

immunity, and long-time measurement [5], and is increasingly applied in cognitive and clinical neuroscience tasks in a daily environment, e.g., localizing the activations of motor, cognitive, language and visual cortex [6]–[9], diagnosing the neurological and psychological disorders [10]–[12], and developing fNIRS-based brain-computer-interfaces (BCIs) [13]–[15].

There are fundamentally three modes of fNIRS-imaging system: time-resolved, frequency-domain and continuous-wave (CW) [2], [3]. Although the former two in principle are capable of assessing the absolute optical properties in tissue, most fNIRS-imaging systems are CW-based, majorly due to two reasons: 1) a CW system are simple in instrumentation and fast in measurement; 2) fNIRS-imaging is most commonly used as a trend monitor and only concerns changes in HbO and Hb concentrations [3]. Primarily, fNIRS-imaging is being accomplished by either the modified-Beer-Lambert-law based optical topography (OT) or the photon-migration-model based diffuse optical tomography (DOT), referred to as fNIRS-OT and -DOT, respectively. Compared to fNIRS-OT that is mathematically robust to topologically provide a less quantitative two-dimensional (2D) hemodynamic map over the domain surface, fNIRS-DOT is more physically consistent to revealing three-dimensional (3D) hemodynamics within the domain and therefore offers the potential to significantly improve the spatial resolution and quantitative accuracy [2]–[4]. However, a successful implementation of fNIRS-DOT relies on many prerequisites, both in instrumentation and algorithm. On the instrumentation side, it is required that the imaging domain is overlappingly sampled by a high-density source-detector array to acquire dense spatial data sets at multiple source-detector separations as well as at multiple wavelengths, and accordingly a high-sensitivity and large-dynamic-range detection technique and a parallel measurement strategy must be designed to achieve acceptable signal-to-noise ratio (SNR) and temporal resolution [3], [4], [16]. On the algorithm side, it is desired that some regularization strategies are applied to mitigate the increased ill-posedness of the inversion and computation burden due to the 3D reconstruction [3], [4], [16].

A wide variety of CW fNIRS-imaging devices have already been commercially available, with their complexity ranging from few sources and detectors suitable to image certain brain regions to high-density (HD) optodes covering whole head [2], [3]. Although devices using sensor patches with integrated components are rapidly advancing towards wireless implementation, most HD systems use optical-fibers-based optodes and flexible head-caps for adaptation to individual subject. Normally, these devices equipped with low power light-emitting-diode (LED) or laser-diode (LD) sources at multiple near-infrared wavelengths and photodiode (PD), avalanche-photodiode (APD) or photomultiplier-tube (PMT) detectors, and adopt either frequency- or code-multiplexing method (or their mixture with time-multiplexing) for distinguishing signals from different emitters and different wavelengths and increasing sampling rate [3]. The systems working with analog-mode APDs/PMTs can achieve high sensitivity but has a moderate dynamic range of $\sim$ 60 dB [17]. Both the sensitivity and dynamic range can be significantly enhanced by the photon counting detection, an effective technique used to detect extremely-low-light at a high dynamic range of $>$100 dB (approximately decided by the ratio of the saturation linear count rate to the dark count rate of the detector) and therefore provide design commitment for adaption of fNIRS instrumentation to DOT implementation as well as its performance optimization for the specific needs of the particular applications, such as investigation of occipital region and development of fast BCIs, *etc*.. Nevertheless, some parallelization strategy could be extended to this discrete mode to ensure a reasonably high temporal resolution, with its feasibility demonstrated in the lock-in photon-counting detection [18], [19].

To this end, ahigh-sensitive and large dynamic prototype CW fNIRS-DOT system is developed in this work, based on the square-wave modulation lock-in photon-counting technique. The instrument possesses 3-wavelengths (785nm, 808nm and 830nm) and 240-channels (20sources $\times$ 12detectors), with each channel achieved with a source of 3-wavelengh LDs, aPMT counting head, and a lock-in photon-counting demodulator of60 digital-phase-detection (PSD) blocks. The design offers frequency-division-multiplexing (FDM) based parallelization of the illumination source and photon-counting based ultrahigh sensitivity of the optical detection. Wehave performed a systematic assessment of the system performances under the practically-viable conditions of the incident power and signal-to-noise ratio, most importantly, thechannel crosstalks - a crucial factor that affects the system parallelization, and accordingly proposed wavelength-switched-multiple-field (WSMF) illumination paradigms for non-overlapping and overlapping measurements, respectively. For evaluation of the overall system performance, DOT experiments have been comparatively conducted on a phantom embedding a practically low-contrasted and deep-sit absorption target, using WSMF illumination paradigm based on non-overlapping and overlapping array, where the topographic absorption-change images over a layer of interest (e.g. the gray layer) were reconstructed using the semi-3D algorithm [20]. The results demonstrate the ability of the system to accurately quantify and localize the target at reasonable time resolution. Also, wehave discussed the ability of the full-3D tomographic scheme to locate and quantify a target using channels with multiple source-detector separations.

## II. INSTRUMENTATION

As sketched in Fig. 1, a highlight in the developed three-wavelength multi-channel CW fNIRS-imaging instrument is the introduction of the lock-in photon-counting technique for a balance among the measurement sensitivity, dynamic-range and temporal resolution, which are three key factors

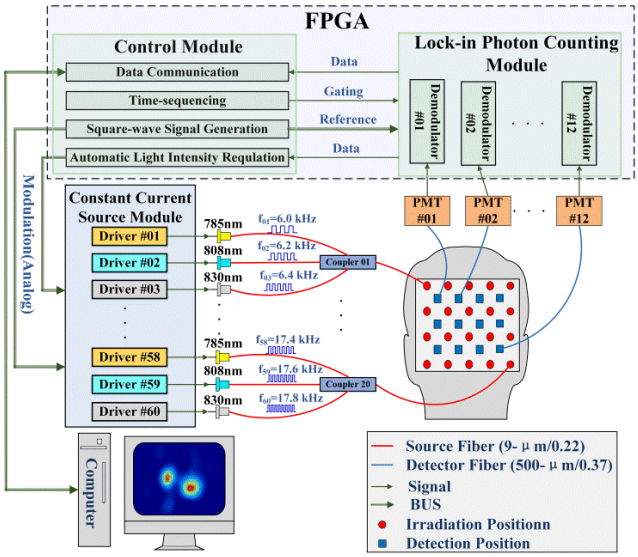


**FIGURE 1.** Schematic of the fNIRS-DOT instrument.

to the high-density fNIRS-DOT implementation. The instrument possesses $S$ (=20) source-optodes and $D$ (=12) detection-optodes. A source-optode bundles $W$ (=3) single-mode fibers with a core diameter of 9-$\mu$m and a numerical aperture ($NA$) of 0.22, connecting to three small power ($\sim$10mW) fiber-tailed LDs at $\lambda_1$(=785 nm ), $\lambda_2$(=808 nm) and $\lambda_3$(=830 nm) wavelengths (Lightsensing, China), respectively. The combination of these wavelengths is widely considered to be optimal for resolving in-vivo changes of hemoglobin [21]–[26]. Corresponding, a constant current source module with $K$(=S$\times$W=60) digitally switchable driver is designed with a bipolar type LD driver ICs (ELM185xB, ELM Technology, Japan) as core components for driving the LDs with functions of stability maintenance, intensity adjustment and modulation. A detection-optode is composed of a single multiple-mode fiber with a core diameter of 500-$\mu$m and NA=0.37, entering to a PMT photon-counting head (H10682-01, Hamamatsu Photonics, Japan), which has a count linearity of $5.0\times10^6$/s and a dark count of 600/s, and thereby a limit dynamic range of $\sim$108 dB. Corresponding to this, a 12-demodulator lock-in photon-counting module is designed based on a field-programmable-gate-array (FPGA) develop kit (DE10, ALTERA), with each demodulator consisting of 60 PSD blocks for a fully parallel demodulation of the 60 signals at a detection position, which originate from the LD illumination of 3 wavelengths at the 20 source positions. The control module is also implemented with the same FPGA, providing modulation signals, time-sequencing, light intensity adjustment and data communication with the instrument computer, which sends the working parameters to and receives the data from the system through LabVIEW programming (National Instruments), as well as reconstructs the images through Matlab programming (MathWorks).

According to the anatomical structure and the optical properties (absorption and scattering) of an adult head, the near infrared light propagation physics decides a source-detector separation of above 30 mm to explore cerebral cortex. The photons would scatter many times and migrate along random paths before being probed by a detector, making the signal very faint. While photon counting is widely accepted as a photoelectric detection mode with ultra-high sensitivity, it has relatively low temporal resolution that is majorly limited by the output electronic pulse width of the PMT photon-counting heads and also by the acceptable SNR of the detected signals for DOT image reconstruction. For a complete measurement of weak light at multiple positions for multiple illuminations, as required in fNIRS-DOT, incorporation of a lock-in technique into the photon-counting detection would enable parallelization of the data-acquisition and therefore substantially increase the temporal resolution to a maximum of that for a single-stimulation collection. As a common knowledge, the lock-in detection also reduces the effect of electrical noise and ambient light [18], [19], [27].

The workflow of the instrument is elaborated as follows: firstly, the working parameters, majorly including source-detector array configuration, illumination paradigm, integration-time ($T_{\text{int}}$) and sampling-period ($T_s$), are transmitted for system setting. Then, the light intensities of the sources are automatically regulated in terms of the source-detector array configuration. Upon being triggered, the lock-in photon-counting processes are temporally sequenced for acquiring a complete frame of the data sets, according to a preset illumination paradigm, i.e., non-overlapping- or overlapping-WSMF. Finally, the data are sent to the instrument computer for image reconstruction.

### A. SQUARE-WAVE MODULATION AND FREQUENCY SELECTION

Although the sine-wave modulation scheme can give lock-in detection an optimal performance in terms of the sensitivity and crosstalk suppression, its implementation has high requirements for the purity of the modulation signals and the modulation linearity of the LD sources. To reduce the system complexity, the square-wave modulation scheme is adopted in this system for the FDM of the sources. In this scheme, the 60 LDs are switched ''ON'' and ''OFF'' by the 60 square-wave modulation signals with a duty cycle of 50% at distinct frequencies, respectively, and meanwhile they are sent to the lock-in photon-counting module as the reference signals of ''$\pm$ 1'' weights for demodulation. Since only digital operations are involved in the demodulation process, no non-linearity error would be introduced, and more importantly, the PSD hardware greatly simplified.

Unlike the sine-wave modulation, frequency selection in the square-wave modulation scheme is a key point. Since, by the Fourier analysis, a square-wave signal with a duty cycle of 50% at a lower frequency is composed of the odd harmonics with their amplitudes decaying by $1/(2n-1)$ ($n$ is the harmonic order), the square-wave modulation signal at a higher frequency should be carefully decided to assure that it does not markedly correlates with the lower frequency

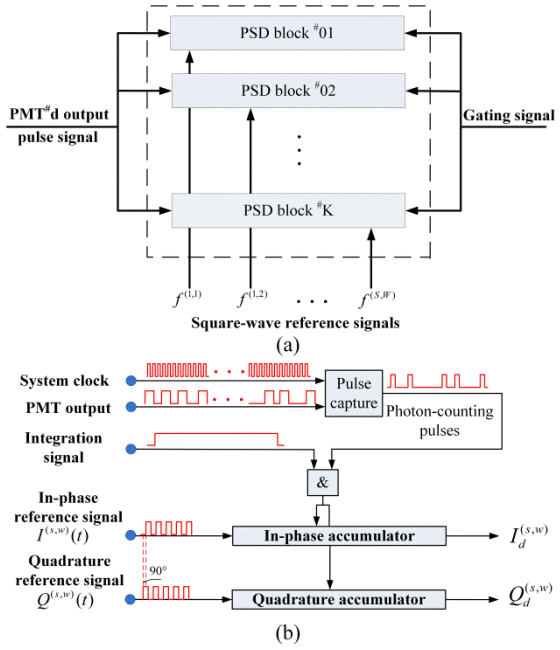


**FIGURE 2.** Schematic of PSD based on RWC strategy: (a) a lock-in photon-counting demodulator and (b) a PSD block.

signals, i.e., the frequencies of the higher frequency signals do not at least coincide with those of the lowest (3rd and/or 5th) order harmonics of the lower frequency signals. With consideration of the harmonic correlation effects as well as the maximum working frequency of the LD driver IC (ELM185xB), i.e., ∼20 kHz, the 60 modulation frequencies used in the system, $f^{(\mathrm{s,w})}$, are chosen with spacing of 200 Hz, in range of 6.0-17.8 kHz.

### B. LOCK-IN PHOTON-COUNTING

The lock-in photon-counting detection is adopted to enable simultaneous multi-wavelength and multi-point illumination, and primarily implemented by the PSD blocks in the system. As illustrated in Fig. 2 (a), each PMT-connected demodulator (with regards to a detection position) in the lock-in photon-counting module is configured with $K$ (=60) PSD blocks to maximally discriminate the component signals at the 60 modulation frequencies (with regards to all the source positions and wavelengths), respectively, from the received composite light signal, which is naturally expressed as superposition of all the square-wave components

$$\Gamma_d(t) = \sum_{s=1}^{S} \sum_{w=1}^{W} \Gamma_d^{(s,w)}(t) \tag{1}$$

where $d(=1, 2, \ldots, D)$ indexes the detectors and $\Gamma_d^{(s,w)}(t)$ denotes the component signal originating from the $s$-th source position at the $w$-th wavelength, *i.e.*,

$$\Gamma_d^{(\mathrm{s,w})}(t) = A_d^{(\mathrm{s,w})} \sum_{n=-\infty}^{+\infty} RECT\left[f^{(\mathrm{s,w})}t + \frac{n}{f^{(\mathrm{s,w})}} + \tau_d^{(s,w)}\right]$$

with $RECT(t) = \begin{cases} 1, & 0 \le \mathrm{t} \le 1/2 \\ 0, & 1/2 \le t < 1 \end{cases}$ being the function of a single canonical square-wave; $A_d^{(\mathrm{s,w})}$ and $\tau_d^{(s,w)}$ indexes the intensity and the initial time-shift, respectively.

In response to a component signal with a specific modulation frequency, the PMT photon-counting head actually outputs the single-electron response (SER) pulses, with an occurrence probability per unit infinitesimal period, $P_d^{(s,w)}(t) \propto \Gamma_d^{(s,w)}(t)$, which is proportional to the instantaneous intensity of the signal. The demodulation of the component signal for acquiring its intensity is achieved by the multi-periodic reference-weighted counting (RWC) strategy in the PSD block, as shown in Fig. 2 (b), where the reference weights at the time of the PMT-SERs output are accumulated for multiple periods.

To eliminate the initial time-shift uncertainty of the signal, a quadrature demodulation scheme is introduced that employs a pair of parallel accumulators to perform the RWC operations with the in-phase and quadrature reference signals, $I^{(s,w)}(t)$ and $Q^{(s,w)}(t)$(90° phase shift), respectively. While these two reference signals originate from the unipolar modulation signal at the same frequency, they are mathematically regarded as bipolar square-wave of "±1" weights in the RWC operations, and can be expressed in terms of the following Fourier series

$$\begin{cases} I^{(s,w)}(t) = \dfrac{4}{\pi} \displaystyle\sum_{n=1}^{\infty} \dfrac{(-1)^{n-1}}{2n-1} \cos[(2n-1)2\pi f^{(s,w)}t] \\ Q^{(s,w)}(t) = \dfrac{4}{\pi} \displaystyle\sum_{n=1}^{\infty} \dfrac{(-1)^{n-1}}{2n-1} \sin[(2n-1)2\pi f^{(s,w)}t] \end{cases} \tag{2}$$

In the discrete regime such as photon counting, the RWC in the digital PSD is mathematically equivalent to the multiplication-integration operations in the conventional analog PSD, where, depending on the reference phase of the PMT-SER occurrences, operation of adding "1" or subtracting "1" is conducted (multiplication) for multiple periods (integration), as illustrated in Fig. 3.

$$\begin{cases} I_d^{(s,w)} = \int_0^{T_{\mathrm{int}}} P_d^{(s,w)}(t) I^{(s,w)}(t) dt \\ \propto \int_0^{T_{\mathrm{int}}} \Gamma_d^{(s,w)}(t) I^{(s,w)}(t) dt \\ = \begin{cases} A_d^{(s,w)}(\frac{1}{2} - 2\tau_d^{(s,w)} f^{(\mathrm{s,w})}), & \tau_d^{(s,w)} \in (0, \frac{1}{2f^{(\mathrm{s,w})}}] \\ A_d^{(s,w)}(2\tau_d^{(s,w)} f^{(\mathrm{s,w})} - \frac{3}{2}), & \tau_d^{(s,w)} \in (\frac{1}{2f^{(\mathrm{s,w})}}, \frac{1}{f^{(\mathrm{s,w})}}] \end{cases} \\ Q_d^{(s,w)} = \int_0^{T_{\mathrm{int}}} P_d^{(s,w)}(t) Q^{(s,w)}(t) dt \\ \propto \int_0^{T_{\mathrm{int}}} \Gamma_d^{(s,w)}(t) Q^{(s,w)}(t) dt \\ = \begin{cases} A_d^{(s,w)}(-2\tau_d^{(s,w)} f^{(\mathrm{s,w})}), & \tau_d^{(s,w)} \in (0, \frac{1}{4f^{(\mathrm{s,w})}}] \\ A_d^{(s,w)}(2\tau_d^{(s,w)} f^{(\mathrm{s,w})} - 1), & \tau_d^{(s,w)} \in (\frac{1}{4f^{(\mathrm{s,w})}}, \frac{3}{4f^{(\mathrm{s,w})}}] \\ A_d^{(s,w)}(2 - 2\tau_d^{(s,w)} f^{(\mathrm{s,w})}), & \tau_d^{(s,w)} \in (\frac{3}{4f^{(\mathrm{s,w})}}, \frac{1}{f^{(\mathrm{s,w})}}] \end{cases} \end{cases} \tag{3}$$

With consideration of the afore-mentioned frequency selection, the RWC process for acquiring the two weighted

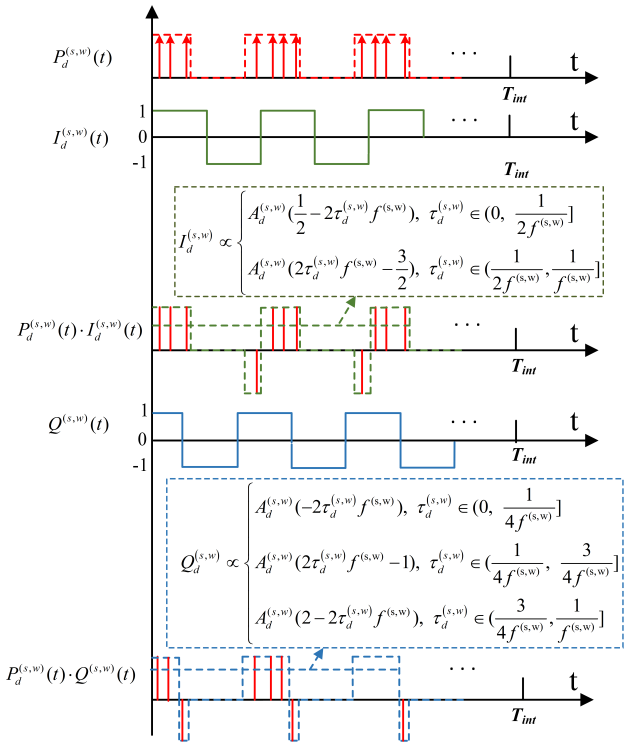


**FIGURE 3.** Diagram of the multi-periodic RWC operation.

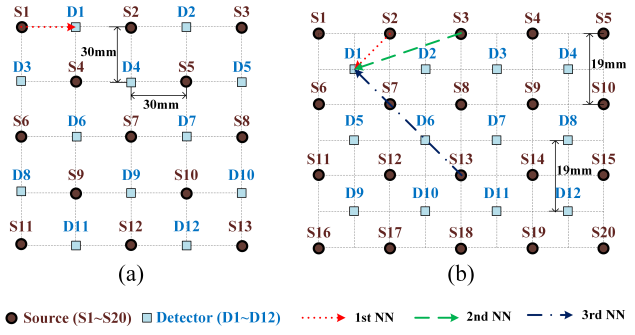


**FIGURE 4.** Two configurations of source-detector array: (a) Non-overlapping measurement and (b) overlapping measurement.

counts of the PMT-SERs, $I_d^{(s,w)}$ (in-phase) and $Q_d^{(s,w)}$ (quadrature), is expressed as above equation (3).

Finally, the photon-count $M_d^{(s,w)}$, can be calculated from the obtained $I_d^{(s,w)}$ and $Q_d^{(s,w)}$ as the measured component signal intensity

$$M_d^{(s,w)} = \left|I_d^{(s,w)}\right| + \left|Q_d^{(s,w)}\right| \propto A_d^{(s,w)} \tag{4}$$

### C. CONFIGURATION OF SOURCE-DETECTOR ARRAY

Configuration of the source-detector array has a direct impact on the spatial resolution and quantitative performance. As shown in Fig. 4, two source-detector array configurations have been employed for non-overlapping and overlapping measurements, respectively.

Application of the non-overlapping configuration with a simple single-grid structure is prevalent in traditional fNIRS-OT [28]. It uses only the 1st nearest neighbor (NN) channels with a single source-detector separation of 30 mm, and therefore can potentially work in a parallel illumination paradigm with negligible channel crosstalks to achieve a high temporal resolution. But, due to sparsity of the source-detector array and incompleteness of the dataset, this configuration intrinsically leads to poor imaging performances in quantitativeness and spatial resolution. On the contrary, the overlapping configuration employs a complex dual-grid structure and works with the 1st-3rd NN channels that have different source-detector separations of 13.4 mm, 30 mm, and 40 mm, respectively [29]. The configuration can provide a complete dataset requested by fNIRS-DOT for improved image quality. It, however, inevitably suffers from conspicuous channel crosstalks, and in most cases has to work in a multiple-field illumination paradigm at a degraded temporal resolution.

### D. AUTO-REGULATION OF LIGHT INTENSITY

It is a common knowledge the practically-viable intensities of the sources depend on both the linear incidence range (saturation counting limit) of the detectors and the maximal irradiation limit for the biological tissue safety. To maintain the above conditions while achieving high SNRs of the detected signals, a function for auto-regulation of the light intensity is necessary to an optimized performance of the system, and implemented in the LD drivers by adjusting the operating current via a digital potentiometer (AD5259, Analog Devices Inc.), whose resistance can be programmed in a range of 0∼5 kΩ at a step of 20 Ω, corresponding to a LD power range of 1∼5 mW. Specific to the employed source-detector array configuration, the different auto-regulation procedures are devised with the criteria that the total photon count-rate at a selected detector should be equally contributed from its illumination sources in the associated most NN channels. i.e., the 1st NN channels for the non-overlapping configuration and the 1st or 2nd NN channels for the overlapping configuration, respectively.

Besides, an overload protection function is designed in the software and hardware to ensure the PMT safety in the auto-regulation process: the maximum intensity threshold in software and power-off protection in hardware.

## III. TOMOGRAPHIC RECONSTRUCTION

In general, the model-based tomographic reconstruction firstly discretizes the domain under consideration, Ω, into voxels (with $N$ nodes), based on which the diffusion equation is numerically solved using the finite-element method (FEM) as the forward model. By optimizing the difference between the measurements from channels of multiple source-detector separations and the corresponding forward predictions as a whole, the spatial distributions of the changes in optical properties within the domain are recovered [30]. Regarding to the task in this work, a linear Born approximation approach is employed to reconstruct the absorption perturbation. The intrinsic 3D inversion can be cast as a solution to the

following matrix equation

$$\mathbf{y} = \mathbf{J} \cdot \delta\boldsymbol{\mu}_a \tag{5}$$

where $\mathbf{y} = [y_{1,1}, y_{1,2}, \ldots, y_{s,d}, \ldots]^T$ numerates the differential measurements of the intensity between the task and rest states for all the used source-detector pairs (channels), and its entries is defined as $y_{s,d} = [M_{s,d}^{(task)} - M_{s,d}^{(rest)}]/M_{s,d}^{(rest)}$, with $M_{s,d}^{(task)}$ and $M_{s,d}^{(rest)}$ denoting the task and rest intensities at the $d$-th detector site for the $s$-th source illumination, respectively. $\delta\boldsymbol{\mu}_a$ lists the absorption changes at the $N$ nodes between the rest and task states. $\mathbf{J}$ is the sensitivity matrix with its elements calculated as

$$\boldsymbol{J}_{s,d,n} = -\frac{\int_\Omega G(\boldsymbol{\xi}_d, \mathbf{r})\Phi(\mathbf{r}, \boldsymbol{\zeta}_s)cu_n(\mathbf{r})d\mathbf{r}}{\Gamma\left(\boldsymbol{\xi}_d, \boldsymbol{\zeta}_s\right)}, \quad n = 1, 2, \ldots, N \tag{6}$$

where $\boldsymbol{\xi}_d$ and $\boldsymbol{\zeta}_s$ indicate the locations of the $d$-th detector and the $s$-th source, $\mathbf{r}$ is the position vector in $\boldsymbol{\Omega}$; $\boldsymbol{\Phi}(\mathbf{r}, \boldsymbol{\zeta}_s)$ is the photon density within the domain from the $s$-th source; $G(\boldsymbol{\xi}_d, \mathbf{r})$ is the Green's function regarding the intensity; $u_n(\mathbf{r})$ is the shape function at the $n$-th node of the discretized domain. $\Gamma(\boldsymbol{\xi}_d, \boldsymbol{\zeta}_s)$ is the model-calculated intensity at the $d$-th detector for the $s$-th source.

In the fNIRS regime, a semi-3D DOT algorithm can be developed instead of the above full-3D one to mitigate the inversion ill-posedness [20], where the absorption changes along the within skin-skull as well as the gray-matter layers can be reasonably assumed invariant along the depth (Z-direction), and the full 3D inversion procedure reduces to a layered 2D form over the cross-sectional domain $\Omega_{xy}$ with $N_{xy}$ node number

$$\mathbf{y} = \begin{bmatrix} \mathbf{J}_{2D}^{skull} & \mathbf{J}_{2D}^{gray} \end{bmatrix} \begin{bmatrix} \delta\boldsymbol{\mu}_a^{skull} \\ \delta\boldsymbol{\mu}_a^{gray} \end{bmatrix} \tag{7}$$

where $\delta\boldsymbol{\mu}_a^{skull} = [\delta\mu_1^{skull}, \delta\mu_2^{skull}, \ldots, \delta\mu_{Nxy}^{skull}]^T$ and $\delta\boldsymbol{\mu}_a^{gray} = [\delta\mu_1^{gray}, \delta\mu_2^{gray}, \ldots, \delta\mu_{Nxy}^{gray}]^T$ represent the 2D distributions of the cross-sectional absorption changes over the skin-skull layer and gray-matter layer, respectively, and their two-dimensional (2D) sensitive matrices, $\mathbf{J}_{2D}^{skull}$ and $\mathbf{J}_{2D}^{gray}$, can be calculated by integrating the 3D one along the corresponding depths of the each layers [20], [31], [32], i.e.

$$J_{s,d,n'}^{v} = \int_v J_{s,d,n} dz \; n' = 1, 2, \ldots, N_{xy} \tag{8}$$

where $v \in \{\text{“}skull\text{”}, \text{“}gray\text{”}\}$ and $N_{xy}$ is number of the 2D nodes over the layers. Equations (5) and (7) can be solved by either the algebraic reconstruction technique (ART) or the regularized least-squares (LS) optimization [30].

## IV. EVALUATIONS OF STSTEM PERFORMANCES

Phantom experiments were firstly conducted for the assessment of the key system performances including the linearity, stability and cross-talks, with the aims of figuring out the optimal operating conditions and measuring configurations to quantify weakly-contrasted absorption changes beneath the skull, as in scenarios of the NIRS brain functional investigation. To eliminate interference influence, a polyformaldehyde cubic phantom of 130 mm (Length)×130 mm (Width)×50 mm (Height) is used to evaluate the system. As shown in Fig. 5(a), the experimental setup adopted an inverted measurement configuration for ease of operation, where a S-D array was placed in contact with the bottom surface of the cubic phantom by a fiber holder. Four cylindrical holes, with the bottom-to-bottom distances of $d = 6, 8, 10$ and 12 mm, respectively, are drilled to mimic the excitation regions at different depths in the task state, as shown in Fig. 5(b).

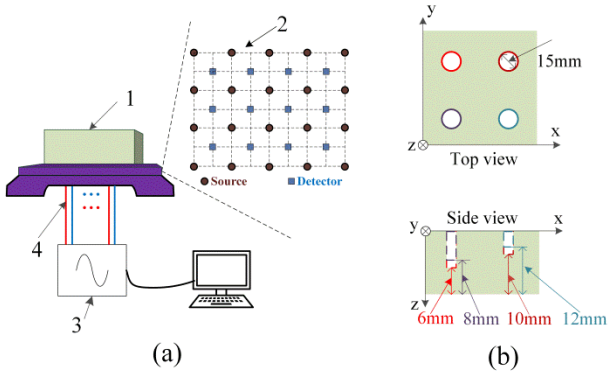


**FIGURE 5.** Phantom experiment: (a) experimental setup, (1)-cubic phantom, (2)-fiber holder, (3)-instrument, and (4) -fibers and (b) phantom profile.

A homogeneous liquid phantom was made from mixture of diluted 20% intralipid and india-ink for filling cylindrical holes. Its background absorption coefficient $\mu_a^{(\mathrm{B})}$ and reduced scattering coefficient $\mu_s'^{(\mathrm{B})}$ were initially set to those of the cerebral cortex at 750-nm, i.e., $\mu_s'^{(\mathrm{B})} = 0.0173mm^{-1}$ and $\mu_s'^{(\mathrm{B})} = 1.0134mm^{-1}$ [33]. Further, the overall imaging ability of the system were experimentally evaluated with the WSMF illumination paradigm for different $d$ and target contrast $C_a = \mu_a^{(T)}/\mu_a^{(B)}$, where $\mu_a^{(T)}$ is the absorption coefficient of the target. As a target, the cylindrical hole with a diameter of 15 mm was filled with higher absorption-contrasted intralipid-india-ink solution.

### A. LINEARITY

The detection linearity at different wavelength was experimentally assessed to verify the validity of the lock-in photon-counting scheme based on square-wave modulation. The S1-D5 channel (2nd NN), as shown in Fig. 4(b), whose source-detector separation was generally considered to probe the cerebral cortex excitation effectively. The output voltage of a PD detector was used to rate the light intensity of S1-LD under different operating currents, for each of which the photon counts demodulated in the referenced PSD block of the D5-PMT lock-in demodulator, all at $T_{int} = 1000$ ms. The LD at different wavelengths illuminated sequentially each irradiation location. In order to ensure the credibility of

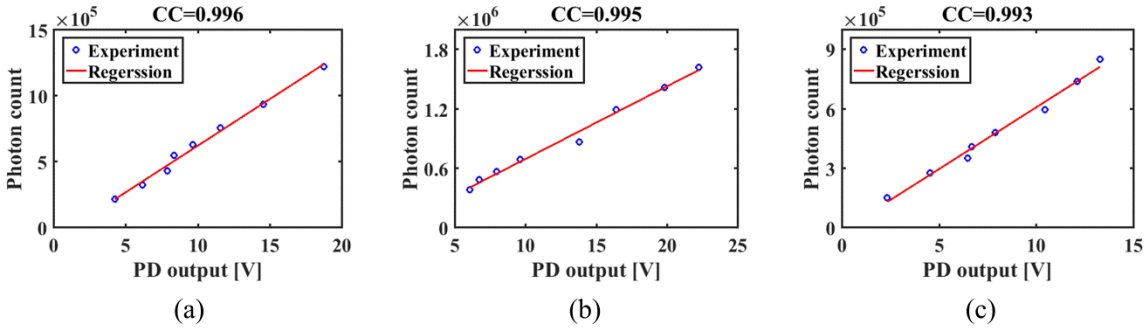


**FIGURE 6.** Linearity assessment by a comparison between the experimental and linearly-regressed data at the working wavelengths of (a) 785 nm, (b) 808 nm, and (c) 830 nm.

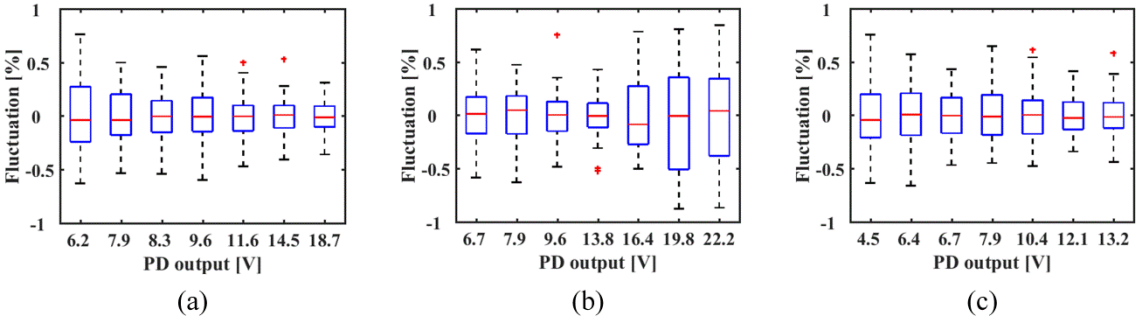


**FIGURE 7.** Fluctuations under different light intensities at the wavelengths of (a) 785 nm, (b) 808 nm, and (c) 830 nm.

the experiment, the average of 10 repeated measurements was calculated for an improved precision.

Fig. 6 plots the demodulated photon counts as a function of the light intensity (PD output). The linear regression analysis (red solid line) of the experimental data shows that the lock-in photon-counting scheme can achieve an excellent detection linearity with the correlation coefficient (CC) of $>0.993$, and the dynamic range of the LD intensity of $>6$, for the three working wavelengths.

### B. STABILITY

It is crucial for all the LDs to secure a long stable operation with the constant current source module. For evaluating stability of the LDs under different light intensities, a series of experiments were conducted at the three wavelengths, using the 2nd NN channel, S1-D5. A metric, referred to as the *fluctuation*, is defined as a function of the sampling serial number, $i$, for the performance quantitation

$$fluctuation(i) = \frac{photon(i) - mean[photon(i)]}{mean[photon(i)]} \times 100\% \quad (9)$$

where $photon(i)$ is the demodulated photon counts at the $i$-th sampling, and $mean[photon(i)]$ calculates the average of all the 60 repeatedly demodulated photon counts.

After warm-up of the system for about 1 hour, the light intensity of the LD was sampled at an interval of 1 min for one hour, all with $T_{int} = 1000$ ms. Figure 7 illustrates the box-plots of the fluctuations for different illumination intensities (PD outputs). It is shown that the photon counts at the three working wavelengths fluctuate within 1% during one hour period.

### C. CROSSTALKS

Although the modulation frequencies have been carefully selected to prevent the interference of higher-order harmonics of a lower frequency signal to a higher frequency signal, the channel cross-talks are still inevitable largely due to the imperfection of the square-wave modulation signals, various noises as well the pulse stacking. The destructive effect of the channel crosstalks is mainly on implementation of the parallel measurement.

To assess this performance, the overlapping ource-detector array configuration is employed, where, as shown in Fig. 8(a), photon counts are evaluated in one of the 2nd NN channels, S3-D7, firstly with only the reference illumination, S3, and then with the interference illuminations, i.e., S4, S7, S10, S12, S15, S18 and S19, successively added, noted as Scenario No. 1-8, respectively. For each illumination scenario, the measurements were repeated for 100 times at 785 nm only, all with $T_{int} = 1000$ ms. The coefficient of variation ($CV$) is defined below as the quantitative measure

$$CV = \frac{std[photon(i)]}{mean[photon(i)]} \times 100\% \quad (10)$$

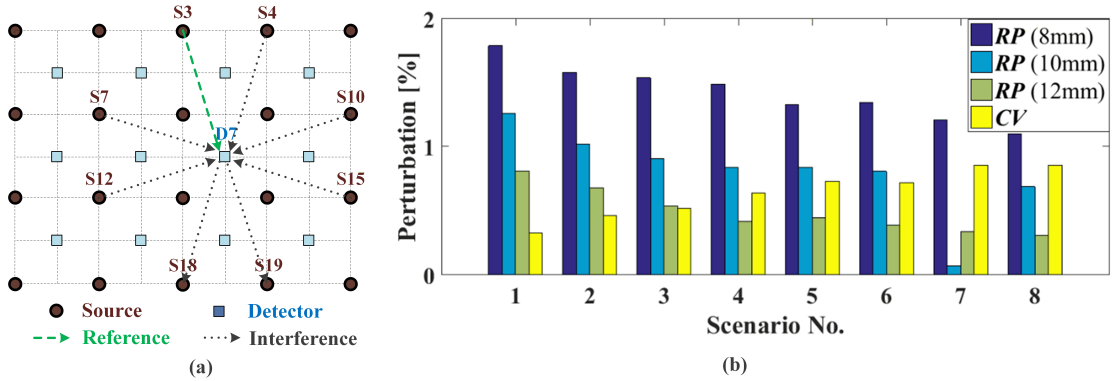


**FIGURE 8.** Crosstalk assessments: (a) source-detector array configuration and experimental protocol and (b) comparisons between *RP*s with different target depths and *CV*s for 8 illumination scenarios.

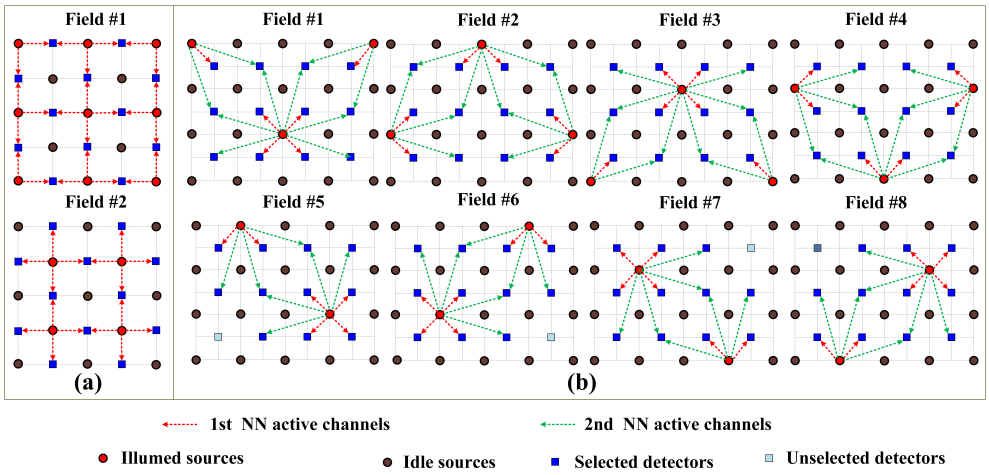


**FIGURE 9.** Progressive fields to realize WSFM illumination paradigms for (a) non-overlapping array using only 1st NN channels and (b) overlapping array using 1st and 2nd NN channels.

where $std[photon(i)]$ and $mean[photon(i)]$ calculate the standard deviation and average count of the 100 repeated measurements, respectively.

In order to quantitatively assess the influence of the channel cross-talks on the imaging performance, an additional experiment was conducted on the phantom with a practically viable target of $C_a = 1.1$ placed at the sampling point (midway point) of the 2nd NN channel, S3-D7, and the reference perturbation ($RP$) is used to measure the intensity variation due to the target, i.e.,

$$RP = \frac{mean[photon_{bg}(i)] - mean[photon_{tg}(i)]}{mean[photon_{bg}(i)]} \times 100\% \quad (11)$$

where $photon_{bg}(i)$ and $photon_{tg}(i)$ denote the $i$-th demodulated photon counts in S3-D7 channel for the background and target phantoms, respectively. $mean[photon_{bg}(i)]$ and $mean[photon_{tg}(i)]$ calculate the average photon count of the 30 repeated measurements for the difference background and target phantom, respectively. As illustrated in Fig. 8(b), the $RP$s with different target depths of $d = 8$, 10 and 12 mm are compared with $CV$s for the 8 illumination scenarios. Since it is possible to detect a target only when $RP$ is greater than $CV$, the observation of the crosstalk assessment provides a reference for selecting a suitable illumination scheme as well as for determining the depth limits of imaging.

## V. IMAGING PERFORMANCE FOR DOT

### A. ILLUMINATION PARADIGM

It is clearly understood from the above assessment that the channel crosstalks bear directly on the illumination scheme and the imaging depth. With consideration of the crosstalk performance, two WSMF illumination paradigms are proposed for the non-overlapping and overlapping source-detector array configurations, respectively, as shown in Fig. 9, with the former progressively covering all the 1st NN channels with two fields and the latter covering all the 1st and 2nd NN channels with eight fields. Both the paradigms follow a criterion that a detector in each field is associated with only two active channels to balance the detection sensitivity, time resolution and imaging depth.

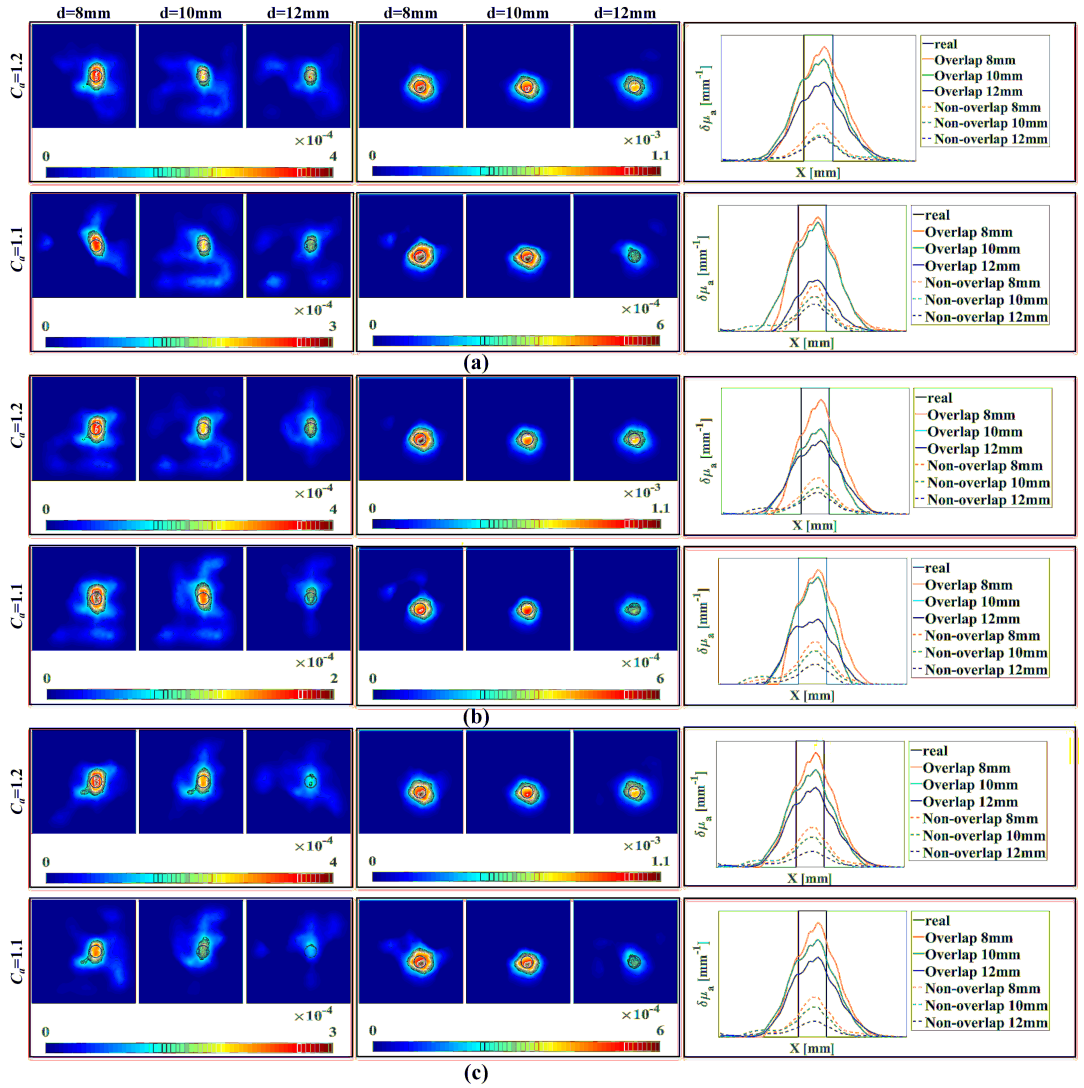


**FIGURE 10.** Phantom experiments: Reconstructed images using the non-overlapping (left) incorporating 1st NN channels and overlapping (middle) incorporating 2nd NN channels measurement, as well as their X-profiles (right), with different depths of $d = 8$ mm, 10 mm 12 mm as well as different target contrasts of $C_a = 1.1$ and 1.2, at (a) 785 nm, (b) 808 nm, and (c) 830 nm, all using $T_{int} = 50$ ms.

### B. PHANTOM VALIDATIONS

The overall imaging performance was experimentally evaluated on the phantom described above, where, at a time, one target-emulating hole was imaged for accessing the sensitivity and quantitativeness of the methodology with low contrasts of $C_a = 1.1$ and $C_a = 1.2$, as well as for confirming the dynamic-range of the instrumentation as using multiple NN channels. A semi-3D DOT algorithm was employed for image reconstruction, where the diffusion equation was solved by the FEM within the phantom volume just above the source-detector array, as the light-propagation model, and a 2D image recovered that integrates the absorption perturbation along the single gray-matter-emulating layer depth (extend upward by 10 mm from the hole bottom). The horizontal profiles passing through the target centers, i.e., the X-profiles, of the images were also presented to compare the reconstructions with different source-detector array configurations.

As illustrated in Fig. 10, the results demonstrate that the system can reliably distinguish a practically contrasted target ($C_a = 1.1$), even using $T_{int} = 50$ ms. The above results were further quantified using the Quantitativeness ($Q$), Spatial Resolution ($SR$) and Contrast-to-Noise Ratio ($CNR$), introduced as follows

$$\begin{cases} Q = \dfrac{mean[\,\delta\mu_a(\mathbf{r})|\,\mathbf{r} \in \Omega_T\,]}{\mu_a^{(T)}} \\ SR = \dfrac{FWHM}{D} \\ CNR = \dfrac{mean[\,\delta\mu_a(\mathbf{r})|\,\mathbf{r} \in \Omega_T\,] - mean[\,\delta\mu_a(\mathbf{r})|\,\mathbf{r} \in \Omega_B]}{std[\,\delta\mu_a(\mathbf{r})|\,\mathbf{r} \in \Omega_B]} \end{cases} \tag{12}$$

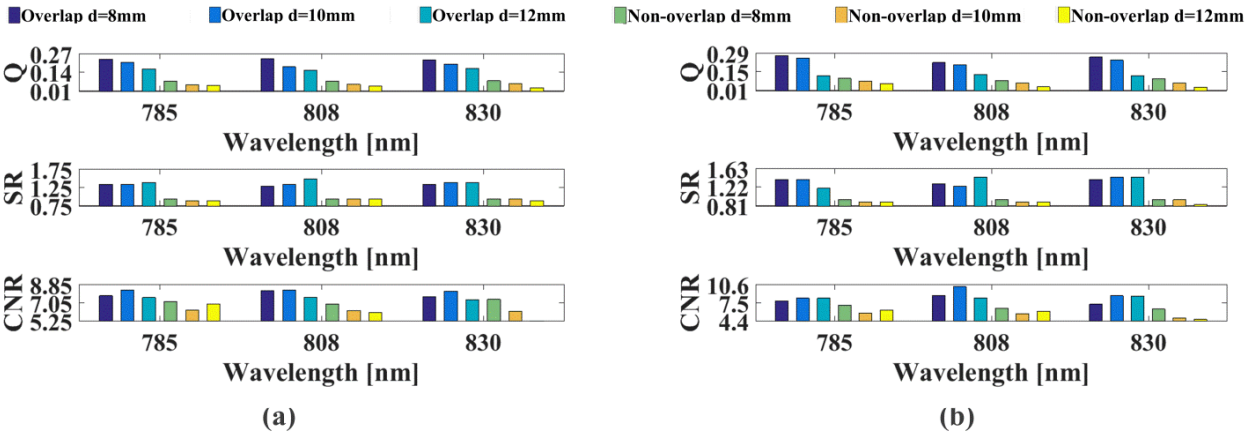


**FIGURE 11.** Quantitative assessments for the reconstructed images using the non-overlapping and overlapping measurement with target contrasts of (a) $C_a = 1.2$ and (b) $C_a = 1.1$.

where, $mean[\delta\mu_a(\mathbf{r})|\,\mathbf{r} \in \Omega_T]$ is the average of the reconstructed absorption change in the target region; *FWHM* denotes the full width at half maximum of the reconstructed target in the X-profile and $D$ is the diameter of the target hole; $mean[\delta\mu_a(\mathbf{r})|\,\mathbf{r} \in \Omega_B]$ and $std[\delta\mu_a(\mathbf{r})|\,\mathbf{r} \in \Omega_B]$ calculate the average and standard deviation of the changes in the background region, respectively. Roughly, $Q$ is employed as an indicator quantitative accuracy of the reconstructed targets, *SR* implies the reconstruction spatial resolution, and *CNR* is defined as a criterion for evaluating the contrast between the reconstructed target and background, i.e., the target visuality. The three measures calculated for the above reconstructed images are illustrated in Fig. 11.

From the calculations, following observations are summarized: Firstly, for the same $C_a$, $Q$ values show a decreasing trend with the increase in $d$, indicating that the signal perturbation is getting weaker with the $d$ increasing; Secondly, for the same $d$, $Q$ decreases with the $C_a$ increasing, demonstrating the saturation effect of DOT reconstruction on increasingly contrasted target as previously observed [34]; Finally, in terms of $Q$ and *SR* measures, the overlapping measurement is overwhelmingly superior to the non-overlapping one. Some unstable trends of CNR are observed which can be ascribed to the low ratio of *RP* to *CV*.

## VI. DISCUSSIONS

Some topics need to be further addressed with regards to the optical property uncertainty of the phantom, advanced application of the proposed illumination paradigms and practical realization, devoting to balancing the temporal resolution, information enrichment and measurement instantaneity.

### A. INFLUENCE OF OPTICAL PROPERTY UNCERTAINTY

It is a rare scenario in practice that the background (baseline) optical properties can be accurately determined. To assess effect of this uncertainty on the reconstruction quality, the semi-3D DOT reconstructions using the above dataset for the case of ($d = 10$mm, $T_{int} = 50$ ms, $\lambda = 785$ *nm*, and $C_a = 1.1$) are performed, as illustrated in Fig. 12, with $\pm 50\%$ deviation in the background optical properties, and compared to that with the exact optical properties.

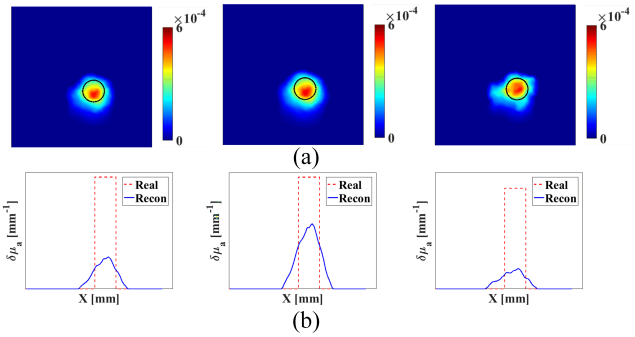


**FIGURE 12.** Influence of optical properties uncertainty on image reconstruction: (a) reconstructed images with baseline (left), −50% deviated (middle) and 50% deviated (right) background optical properties and (b) their X-profiles.

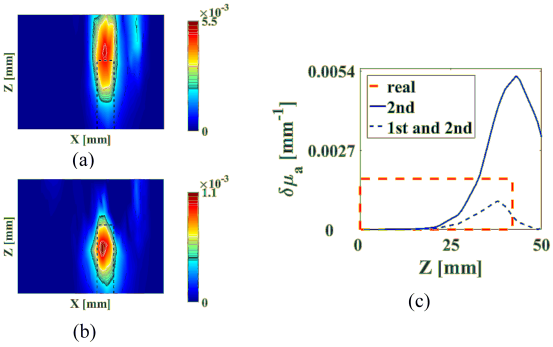


**FIGURE 13.** 3D reconstructions: (a) X-Z images using the 2nd NN channel data, (b) X-Z images using the 1st and 2nd NN channel data, and (c) Z-profiles, all through the target center.

The results show that the background optical parameters deviation has a marginal effect on location but an evident

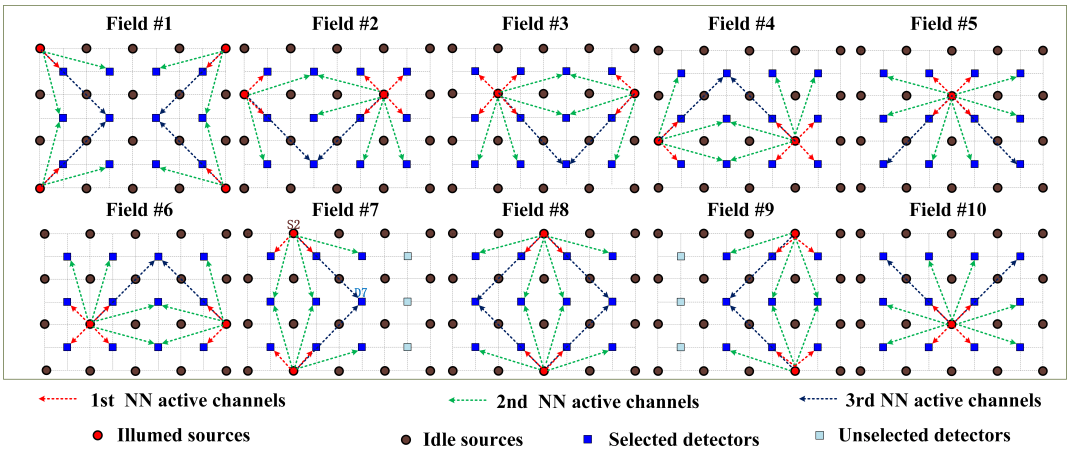


**FIGURE 14.** An illumination paradigm using overlapping source-detector array for simultaneously sampling 1st - 3rd NN channels.

effect on quantification of the absorption changes. Nevertheless, a reasonable conjecture can be deduced that the methodology and system has the capacity to identify the faint nerve excitation even subjects with quite different background optical properties.

### B. UTILIZIATION OF MULTIPLE NN CHANNELS

The effective depth of detection varies in terms of different source-detector separations that probe different brain-layers. In practice, the 2nd NN channels have been playing a more important role in neuroimaging, benefitting from reasonable SNR and effective detection depth concerning the cerebral layer. In the above experiments, the semi-3D DOT algorithm that uses only the 2nd NN channel data is developed to significantly reduce the unknowns by incorporating the priori information on the activation layer position as well as assumption that the absorption perturbation is invariant along the depth direction. Nevertheless, many studies suggest that the task-related hemodynamics and physiological noises may induce the absorption perturbation in the scalp in addition to the cerebral cortex (gray matter) [35], [36]. In view of this fact, it is necessary to extend the proposed semi-3D algorithm for the double layer reconstruction or develop a full-3D method that enables depth resolution [32], [37].

For a proof-of-concept demonstration of the full-3D algorithm, the reconstructions ($d = 8$mm, $T_{int} = 50$ ms $\lambda = 785$ *nm*, and $C_a = 1.1$) using only the 2nd NN channel data and both the 1st and 2nd NN channel data were comparatively performed using the $L_1$-norm regularized LS scheme, with their X-Z cross-sectional images and Z-profiles illustrated in Fig. 13.

The results clearly indicate that the multiple NN channel data can be synergistically employed to improve the localization and quantitation accuracy of the target as well as the depth resolution of the reconstructed image. Additionally, Figure 14 presents an additional WSMF illumination paradigm for the overlapping source-detector measurement

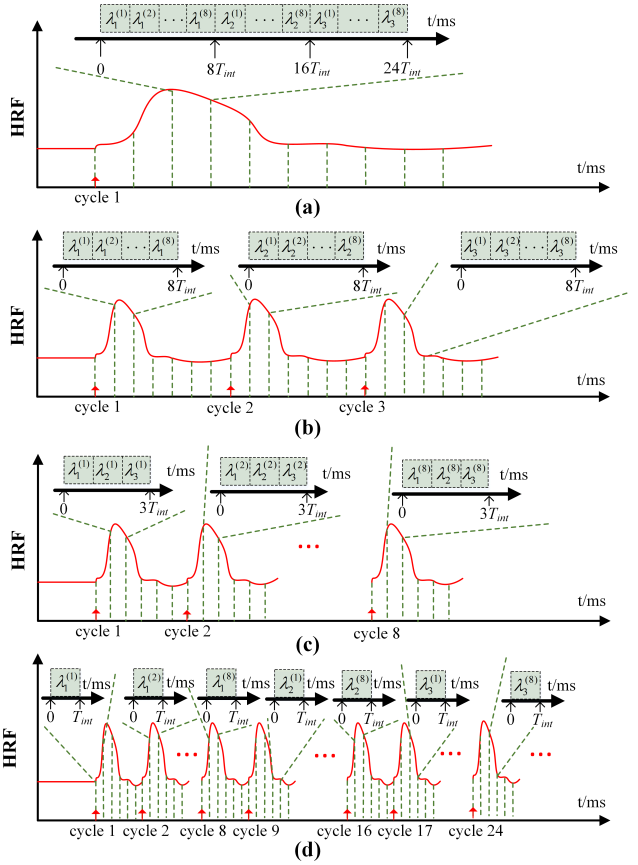


**FIGURE 15.** Realization for overlapping-WSMF measurement paradigm: (a) scheme A, (b) scheme B, (c) scheme C, and (d) scheme D. $\lambda_1^{(i)}$, $\lambda_2^{(i)}$ and $\lambda_3^{(i)}$ indicate the i-th field at three wavelengths of 785 nm, 808 nm and 830 nm, respectively.

array, which employs 10 fields of a frame to simultaneously collect the 1st-3rd NN channels information. This scheme is expected to have a potential to provide information in more depth or further refine the spatial resolution in the reconstruction.

**TABLE 1. Specifications of different measurement paradigm schemes.**

| Scheme | A | B | C | D |
|---|---|---|---|---|
| Time resolution ($\times T_{int}$) | 24 | 8 | 3 | 1 |
| Stimulation cycles | 1 | 3 | 8 | 24 |

### C. REALIZATION OF WSMF PARADIGMS

Although the WSMF measurement paradigms undoubtedly improve the sensitivity by restricting the channel crosstalks from only two neighboring active channels, it is achieved at the cost of lower temporal resolution, as shown Fig. 15(a).

In this original scheme of the WSMF paradigm for the overlapping source-detector array, namely Scheme A, Only one stimulation cycle is needed and the measurement at a sampling point contains a complete set of the successive integrations for the n fields at 3 wavelengths. The scheme works at a low temporal resolution of $3\times8\times T_{int}$. A solution to this issue is to distribute the measurement for a complete set of the multiple fields and multiple wavelengths over repetitive stimulation cycles, as illustrated in Fig. 15(b)-(d), namely Scheme B-D. Scheme B requires 3 repetitive stimulation cycles and the measurement at a sampling point is performed for the n fields at a single wavelength per cycle. An improved temporal resolution of $8\times T_{int}$ is achieved. Scheme C employs n repetitive stimulation cycles and the measurement at a sampling point is conducted at the three wavelengths for a single field per cycle, reducing the temporal resolution to $3\times T_{int}$. In Scheme D, the temporal resolution decreases to $T_{int}$ by performing the measurement at a sampling point for a single field at a single wavelength per cycle. This scheme maximally employs $3 \times 8$ repetitive stimulation cycles. Table 1 lists the specifications of the above schemes. The ultimate time resolutions are calculated to be 1200 ms, 400 ms, 150 ms and 50 ms for Scheme A-D, respectively, based on the experimentally viable time integration of $T_{int} = 50$ ms.

It is worth pointing out that, for all the schemes, the temporal resolution can be reduced to one over $n$ by increasing the simulation cycles $n$ times.

## VII. CONCLUSION

A high-density CW fNIRS system is proposed for brain functional DOT with a configuration of 3 wavelengths and 240 channels (20 sources and 12 detectors). The system potentially achieves multi-channel parallel measurement based on the lock-in photon-counting detection of square-wave modulation mode, enabling high sensitivity, large dynamic range and temporal resolution. The comprehensive assessments of the system have been experimentally conducted on a solid-liquid phantom and show its excellent performances in the detection linearity, source stability and channel cross-talks. Furthermore, the WSMF measurement paradigms have been implemented for the non-overlapping and overlapping source-detector array configurations with varying sensitivity and temporal resolution. The image reconstructions using the semi-3D DOT algorithm with different $T_{int}$ and $C_a$ have validated the ability of the methodology to accurately locate activation region with a promising sensitivity ($C_a = 1.1$) and a reasonably temporal resolution ($T_{int} = 50$ ms). In particular, a brilliant reconstruction quality with the high contrast and limited artifacts has enforced the overall evaluation of the system using the WSMF illumination paradigms for the overlapping configuration. It is no doubt that the WSMF paradigms effectively reduce the cross-talks in the counting channels, and different realizations of measurement paradigm schemes go closer to clinical neuroimaging.

In general, the developed CW fNIRS-DOT instrument can reliably quantify cerebral cortex activation level, and also be used as a highly-sensitive and dynamic acquisition system for tissue heterogeneity detection and oxygen metabolism in breast cancer, as well as in pharmacokinetic imaging for specificity enhancement. With the aid of a suitable DOT algorithm it possibly opens a new route for the biomedical optical imaging in macro-scale.

## REFERENCES

[1] F. F. Jöbsis, "Noninvasive, infrared monitoring of cerebral and myocardial oxygen sufficiency and circulatory parameters," *Science*, vol. 198, no. 4323, pp. 1264–1267, 1977.
[2] M. Ferrari and V. Quaresima, "A brief review on the history of human functional near-infrared spectroscopy (fNIRS) development and fields of application," *NeuroImage*, vol. 63, no. 2, pp. 921–935, 2012.
[3] F. Scholkmann, S. Kleiser, A. J. Metz, R. Zimmermann, J. M. Pavia, U. Wolf, and M. Wolf, "A review on continuous wave functional near-infrared spectroscopy and imaging instrumentation and methodology," *NeuroImage*, vol. 85, no. 1, pp. 6–27, Jan. 2014.
[4] Y. Hoshi, "Towards the next generation of near-infrared spectroscopy," *Philos. Trans. Roy. Soc. A, Math., Phys. Eng. Sci.*, vol. 369, no. 1995, pp. 4425–4439, 2011.
[5] J. C. Ye, S. Tak, K. E. Jang, J. Jung, and J. Jang, "NIRS-SPM: Statistical parametric mapping for near-infrared spectroscopy," *NeuroImage*, vol. 44, no. 2, pp. 428–447, 2009.
[6] S. R. Hintz, D. A. Benaron, A. M. Siegel, A. Zourabian, D. K. Stevenson, and D. A. Boas, "Bedside functional imaging of the premature infant brain during passive motor activation," *J. Perinatal Med.*, vol. 29, no. 4, pp. 335–343, 2001.
[7] N. Liu, X. Cui, D. M. Bryant, and G. H. Glover, "Inferring deep-brain activity from cortical activity using functional near-infrared spectroscopy," *Biomed. Opt. Express*, vol. 6, no. 3, pp. 1074–1089, 2015.
[8] J. Li and L. Qiu, "Temporal correlation of spontaneous hemodynamic activity in language areas measured with functional near-infrared spectroscopy," *Biomed. Opt. Express*, vol. 5, no. 2, pp. 587–595, 2014.
[9] S. Wijeakumar, U. Shahani, W. A. Simpson, and D. L. McCulloch, "Localization of hemodynamic responses to simple visual stimulation: An fNIRS study," *Invest. Ophthalmol. Vis. Sci.*, vol. 53, no. 4, pp. 2266–2273, 2012.
[10] F. Irani, S. M. Platek, S. Bunce, A. C. Ruocco, and D. Chute, "Functional near infrared spectroscopy (fNIRS): An emerging neuroimaging technology with important applications for the study of brain disorders," *Clin. Neuropsychol.*, vol. 21, no. 1, pp. 9–37, 2007.
[11] H. Obrig and J. Steinbrink, "Non-invasive optical imaging of stroke," *Phil. Trans. Roy. Soc. A, Math., Phys. Eng. Sci.*, vol. 369, no. 1955, pp. 4470–4494, 2012.
[12] A. C. Ehlis, S. Schneider, T. Dresler, and A. J. Fallgatter, "Application of functional near-infrared spectroscopy in psychiatry," *NeuroImage*, vol. 85, pp. 478–488, Jan. 2014.
[13] S. M. Coyle, T. E. Ward, and C. M. Markham, "Brain–computer interface using a simplified functional near-infrared spectroscopy system," *J. Neural Eng.*, vol. 4, no. 3, pp. 219–226, 2007.
[14] N. Naseer and K. S. Hong, "fNIRS-based brain-computer interfaces: A review," *Frontiers Hum. Neurosci.*, vol. 9, no. 3, pp. 1–15, 2015.
[15] S. Weyand, L. Schudlo, K. Takehara-Nishiuchi, and T. Chau, "Usability and performance-informed selection of personalized mental tasks for an online near-infrared spectroscopy brain-computer interface," *Neurophotonics*, vol. 2, no. 2, 2015, Art. no. 025001.

[16] A. T. Eggebrecht, S. L. Ferradal, A. Robichaux-Viehoever, M. S. Hassanpour, H. Dehghani, A. Z. Snyder, T. Hershey, and J. P. Culver, "Mapping distributed brain function and networks with diffuse optical tomography," *Nature Photon.*, vol. 8, no. 6, pp. 448–454, 2014.
[17] G. Strangman, D. A. Boas, and J. P. Sutton, "Non-invasive neuroimaging using near-infrared light," *Biol. Psychiatry*, vol. 52, no. 7, pp. 679–693, 2002.
[18] A. Restelli, R. Abbiati, and A. Geraci, "Digital field programmable gate array-based lock-in amplifier for high-performance photon counting applications," *Rev. Sci. Instrum.*, vol. 76, Jul. 2005, Art. no. 093112.
[19] W. Chen, X. Wang, B. Wang, Y. Wang, Y. Zhang, H. Zhao, and F. Gao, "Lock-in-photon-counting-based highly-sensitive and large-dynamic imaging system for continuous-wave diffuse optical tomography," *Biomed. Opt. Express*, vol. 7, no. 2, pp. 499–511, 2016.
[20] F. Gao, Y. Tanikawa, H. J. Zhao, and Y. Yamada, "Semi-three-dimensional algorithm for time-resolved diffuse optical tomography by use of the generalized pulse spectrum technique," *Appl. Opt.*, vol. 41, no. 34, pp. 7346–7358, 2002.
[21] A. Corlu, T. Durduran, R. Choe, M. Schweiger, E. M. C. Hillman, S. R. Arridge, and A. G. Yodh, "Uniqueness and wavelength optimization in continuous-wave multispectral diffuse optical tomography," *Opt. Lett.*, vol. 28, no. 23, pp. 2339–2341, 2003.
[22] A. Corlu, R. Choe, T. Durduran, K. Lee, M. Schweiger, S. R. Arridge, E. M. C. Hillman, and A. G. Yodh, "Diffuse optical tomography with spectral constraints and wavelength optimization," *Appl. Opt.*, vol. 44, no. 11, pp. 2082–2093, 2005.
[23] M. Eames, J. Wang, B. W. Pogue, and H. Dehghani, "Wavelength band optimization in spectral near-infrared optical tomography improves accuracy while reducing data acquisition and computational burden," *J. Biomed. Opt.*, vol. 13, no. 5, 2008, Art. no. 054037.
[24] T. M. Correia, A. P. Gibson, and J. C. Hebden, "Identification of the optimal wavelengths for optical topography: A photon measurement density function analysis," *J. Biomed. Opt.*, vol. 15, no. 5, 2010, Art. no. 056002.
[25] M. A. Mclntosh, U. Shahani, R. G. Boulton, and D. L. Mcculloch, "Absolute quantification of oxygenated hemoglobin within the visual cortex with functional near infrared spectroscopy (fNIRS)," *Invest. Ophthalmol. Vis. Sci.*, vol. 51, no. 9, pp. 4856–4860, 2010.
[26] D. G. Wyser, O. Lambercy, F. Scholkmann, M. Wolf, and R. Gassert, "Wearable and modular functional near-infrared spectroscopy instrument with multidistance measurements at four wavelengths," *Neurophotonics*, vol. 4, no. 4, 2017, Art. no. 041413.
[27] D. Braun and A. Libchaber, "Computer-based photon-counting lock-in for phase detection at the shot-noise limit," *Opt. Lett.*, vol. 27, no. 16, pp. 1418–1420, 2002.
[28] H. Koizumi, T. Yamamoto, A. Maki, Y. Yamashita, H. Sato, H. Kawaguchi, and N. Ichikawa, "Optical topography: Practical problems and new applications," *Appl. Opt.*, vol. 42, no. 16, pp. 3054–3062, 2003.
[29] D. A. Boas, K. Chen, D. Grebert, and M. A. Franceschini, "Improving the diffuse optical imaging spatial resolution of the cerebral hemodynamic response to brain activation in humans," *Opt. Lett.*, vol. 29, no. 13, pp. 1506–1508, 2004.
[30] R. S. Arridge, "Optical tomography in medical imaging," *Inverse Problems*, vol. 15, no. 2, pp. R41–R93, 1999.
[31] F. Gao, H. J. Zhao, Y. Tanikawa, and Y. Yamada, "Optical tomographic mapping of cerebral haemodynamics by means of time-domain detection: Methodology and phantom validation," *Phys. Med. Biol.*, vol. 49, no. 6, pp. 1055–1078, 2004.
[32] B. Wang, T. Pan, Y. Zhang, D. Liu, J. Jiang, H. Zhao, and F. Gao, "A Kalman-based tomographic scheme for directly reconstructing activation levels of brain function," *Opt. Express*, vol. 27, no. 3, pp. 3229–3246, 2019.
[33] A. T. Eggebrecht, B. R. White, S. L. Ferradal, C. Chen, Y. Zhan, A. Z. Snyder, H. Dehghani, and J. P. Culver, "A quantitative spatial comparison of high-density diffuse optical tomography and fMRI cortical mapping," *NeuroImage*, vol. 61, no. 4, pp. 1120–1128, 2012.
[34] F. Gao, H. J. Zhao, Y. Tanikawa, K. Homma, and Y. Yamada, "Influences of target size and contrast on near infrared diffuse optical tomography—A comparison between featured-data and full time-resolved schemes," *Opt. Quantum Electron.*, vol. 37, nos. 13–15, pp. 1287–1304, 2005.
[35] Y. Zhang, X. Liu, D. Liu, C. Yang, Q. Wang, J. Sun, and K. Wang, "Evoked hemodynamic response estimation to auditory stimulus using recursive least squares adaptive filtering with multidistance measurement of near-infrared spectroscopy," *J. Healthcare Eng.*, vol. 2018, Mar. 2018, Art. no. 7609713.
[36] T. Sato, I. Nambu, K. Takeda, T. Aihara, O. Yamashita, Y. Isogaya, Y. Inoue, Y. Otaka, Y. Wada, M. Kawato, M.-A. Sato, and R. Osu, "Reduction of global interference of scalp-hemodynamics in functional near-infrared spectroscopy using short distance probes," *NeuroImage*, vol. 141, pp. 120–132, Nov. 2016.
[37] X. Wu, A. T. Eggebrecht, S. L. Ferradal, J. P. Culver, and H. Dehghani, "Evaluation of rigid registration methods for whole head imaging in diffuse optical tomography," *Neurophotonics*, vol. 2, no. 3, 2015, Art. no. 035002.

**DONGYUAN LIU** received the B.S. and M.S. degrees in electronic information engineering from Tianjin Polytechnic University, in 2013 and 2017, respectively. He is currently pursuing the Ph.D. degree in biomedical engineering with Tianjin University. His research interests include instrumentation and the algorithm development of functional brain imaging.

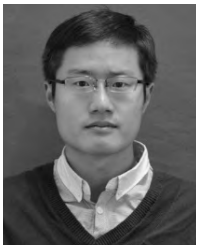

**BINGYUAN WANG** was born in 1988. He is currently pursuing the Ph.D. degree in biomedical engineering with the College of Precision Instrument and Optoelectronics Engineering, Tianjin University, Tianjin, China. His research interests include diffuse optical tomography, near-infrared spectroscopy, weak light detection, and sparsity regularization methods.

**TIANTIAN PAN** was born in Nantong, Jiangsu, China, in 1995. She received the B.S. degree in biomedical engineering from the University of Shanghai for Science and Technology, in 2017. She is currently pursuing the M.S. degree in biomedical engineering with Tianjin University. Her research interest includes instrumentation and algorithm development of functional brain imaging.

**JIAO LI** was born in 1986. She received the B.S., M.S., and Ph.D. degrees in biomedical engineering from Tianjin University, China, in 2008, 2010, and 2013, respectively, where she is currently an Associate Professor with the College of Precision Instrument and Optoelectronics Engineering. Her research interests include photo-acoustic imaging, biomedical optical imaging, and optical detection technique.

**ZHUANPING QIN** received the bachelor's and master's degrees from the Hebei University of Technology, in 2006 and 2009, respectively, and the Ph.D. degree from Tianjin University, in 2013, all in biomedical engineering. Since 2013, she has been with the Tianjin University of Technology and Education. She has authored or coauthored over 20 papers in journals and conference proceedings. Her research interests include biomedical photonics and medical imaging.

**LIMIN ZHANG** was born in 1980. She received the B.S. degree from Hebei Normal University, in 2003, and the Ph.D. degree from Tianjin University, China, in 2009, where he is currently an Associate Professor with the College of Precision Instrument and Optoelectronics Engineering. She was the Project Leader of the Tianjin Key Laboratory of Biomedical Detecting Techniques and Instruments. Her research interests include biomedical photonics, biomedical optical imaging, and optical detection technique.

**ZHONGXING ZHOU** received the bachelor's, master's, and Ph.D. degrees in biomedical engineering from the School of Precision Instrument and Optoelectronics Engineering, Tianjin University, in 2003, 2006, and 2009, respectively, where he has been an Associate Professor in biomedical engineering, since 2012. He has authored or coauthored over 50 papers in journals and conference proceedings. He currently holds 16 patents. His research interests include advanced X-ray imaging techniques, medical imaging, and biomedical signal processing.

**FENG GAO** received the bachelor's and master's degrees in radio technology from Xian Jiaotong University, in 1985 and 1988, respectively, and the Ph.D. degree in physical electronics from the Xi'an Institute of Optics and Precision Mechanics, Chinese Academy of Sciences, in 1998. Since 2004, he has a full-time Professor in biomedical engineering with Tianjin University. He has authored or coauthored over 280 papers in journals and conference proceedings, and four books. He currently holds 16 patents. His research interests include biomedical photonics, medical imaging, and photoelectric detection.